Available online at www.sciencedirect.com

jmr&t Journal of Materials Research and Technology

journal homepage: www.elsevier.com/locate/jmrt

Original Article

Effects of different cooling rates on the microstructure, crystallographic features, and hydrogen induced cracking of API X80 pipeline steel

Mario F.G. Ramirez [a], José W.C. Hernández [b], Duberney H. Ladino [c], Mohammad Masoumi [d,*], Helio Goldenstein [b]

[a] Facultad de Ingeniería, Universidad Santiago de Cali – Campus Pampalinda, Calle 5 N. 62, Cali, Valle del Cauca, Colombia

[b] Departamento de Engenharia Metalúrgica e de Materiais e Escola Politecnica da Universidade de Sao Paulo e EPUSP/PMT, Av. Professor Mello Moraes, Sao Paulo, SP, Brazil

[c] Facultad de Ingeniería Mecánica, Campus Aguas Claras, Cra 22 con Calle 1 Vía a Puerto López, Villavicencio, Colombia

[d] Centro de Engenharia, Modelagem, e Ciências Sociais Aplicadas, Universidade Federal Do ABC, Santo, André, SP, 09210-580, Brazil

ARTICLE INFO

Article history:
Received 29 March 2021
Accepted 11 July 2021
Available online 21 July 2021

Keywords:
HSLA
Electron backscattered diffraction
Strain distribution
Grain orientation
HIC

ABSTRACT

Hydrogen-Induced Cracking (HIC) is a primary failure mechanism of pipeline-welded joints in the absence of external loading in the oil and gas exploration industries. Three different cooling rates after austenitization were used to simulate in the laboratory different regions of the heat-affected zone (HAZ) formed when welding an API X80 pipeline steel specially designed to enhance the HIC resistance. The samples were characterized with regard to microstructure and crystallography as well as HIC resistance. The HIC resistance test used NACE TM0284-2011 methodology. The microstructure and its homogeneity varied as a function of cooling rates. Samples containing inclusions and segregation zone from the segregation bands of specimens showed reduced HIC resistance, while specimens containing only acicular ferrite and granular bainite coupled with the absence of segregation zone showed significant improvement in HIC resistance. The best HIC resistance results came from samples presenting fine acicular ferrite consisting of fine interlocking plates, with divergent crystallographic orientations, preventing the formation of localized strain distribution inside the grain and at grain boundaries. It was also found that a large proportion of medium-angle boundaries prevent microcrack initiation and the transgranular mode of crack propagation.

* Corresponding author.
E-mail address: mohammad.m@ufabc.edu.br (M. Masoumi).

https://doi.org/10.1016/j.jmrt.2021.07.060

1. Introduction

High strength low alloy (HSLA) steels are widely used in oil and natural gas transportation due to the high combination of strength and toughness. Welding the pipe sections together on site is essential for manufacturing pipelines to transport oil and natural gas from extraction to the refineries. The heat input involved in the welding process can alter the original microstructure, leading to the formation of a fusion zone and heat-affected zones (HAZs), which can reduce the service life period due to changes in mechanical properties. The coarse-grained heat-affected zone (CGHAZ) and the intercritical reheated coarse-grained heat-affected zone (ICRCGHAZ) formed by welding are the two main HAZ regions with the lowest mechanical and toughness properties, which accelerate the cleavage mode of brittle failure [1,2]. Grain growth, the formation of segregation and precipitates, and bainite and martensite phases formation can deteriorate the mechanical and corrosion resistance properties, especially in the HAZ region. On the other hand, the dispersion of martensite-austenite (M-A) constituents along prior austenite grains (PAGs) boundaries can promote micro-cracks initiation, although crack susceptibility can vary depending of the matrix, hardness of (M-A), and (M-A)/matrix interface, and therefore, depending on the (M-A) characteristics, can suppress crack propagation.

The researchers documented that HIC susceptibility strongly depends on the type and morphology of inclusions [3,4]. Qi et al. [3] showed that spherical Al-, Si-, and Ca–Al–O–S enriched inclusions are highly prone to HIC as well. Hejazi et al. [4] reported that aluminum oxide, aluminum-calcium-silicon-oxide promote HIC susceptibility. Structural defects such as inclusion and precipitates promote crack nucleation by generating a high stress concentration. Then, cracking easily propagates along grain boundaries and hard phases and precipitates/matrix interface. Microstructure also plays a significant role in crack propagation. For instance, hard phases such as martensite and bainite facilitate crack propagation. Venegas et al. [5] investigated the effect of crystallographic textures and grain–boundary distributions to increase HIC resistance. They found that dominant {111} grain oriented along rolling planes (RP) can improve HIC resistance. Mohtadi-Bonab et al. [6] reported that grain boundaries associated with {001}//RP grains provide an easy path for crack propagation. Masoumi et al. [7,8] investigated the effect of grain boundaries on HIC susceptibility of API X70 steel. They showed that high angle grain boundaries provide preferred crack paths in intergranular crack propagation, while these grains act as crack propagation barriers in transgranular crack propagation mode, increasing the fracture toughness and HIC resistance.

Welded joints in H_2S environments are highly prone to hydrogen induced cracking due to the penetration of atomic hydrogen through the steel during operational service. The nucleation and propagation of HIC cracks are strongly dependent on the type, geometry, distribution, and chemical composition of inclusions and micro-constituents [9]. Park et al. [10] compared the hydrogen trapping efficiency in different microstructures for API X65 grade pipeline steel. The hydrogen trapping and hydrogen diffusion are gradually increased in the order of degenerated pearlite, bainite, and acicular ferrite. The hydrogen trapping efficiency at the M-A constituents is much higher than other phases, leading to more HIC sensitivity. Arora et al. [2] investigated the influence of thermal cycles of the CGHAZs on microstructure evolution and their effects on impact toughness of the dissimilar API X65 and X80 weld joints. They reported the presence of ferrite and pearlite phases in X65 steel, while M-A constituents were developed within the grain and along the prior austenite grain size (PAGS) boundaries of X80 steel, causing brittle failure and a slight drop in the Charpy impact toughness. Mohammadijoo et al. [1] also reported M-A constituents had detrimental effect on the deterioration of mechanical and corrosion properties by accelerating the micro-cracks initiation and propagation. Saffari et al. [11] investigated the effect of carbon diffusion from the base metal to the welding pool of API 5 L X65/AISI 304 dissimilar joint by electron backscattering diffraction (EBSD), X-Ray diffraction (XRD) to understand the formation of a hard martensitic layer as a crack initiation source. The EBSD technique was used at the interface of the base metal and the weld zone to analyze grain orientation and distribution of high angle grain boundary between dendrites with different orientations. Omale et al. [12] highlighted the role of crystallographic orientation on hydrogen induced cracking and stress corrosion cracking in API 5 L X70 pipeline steel welded joints. They reported that the formation of bainite sheaves at the prior austenite grain boundaries surrounded by carbides by controlling the cooling rate, associated with the Goss ({001}<100>), brass ({110}<112>) texture, significantly improves HIC resistance. Then, Avila et al. [13] reported that the boundaries with misorientation angles above 45° are attributed to the bainite packets with irregular and straight ferrite plates, presenting barriers to crack growth.

The present paper aims to investigate the effect of cooling rates on austenite transformation products developed in the HAZ zone and their effect on HIC resistance. Three different cooling rates at austenitization temperature were designed to investigate the effect of different obtained microstructure morphologies on the HIC resistance of the welded API X80 pipeline steel. The influence of non-metallic inclusions on micro-crack initiation and crack propagation was also studied. Finally, the effect of crystallographic features (i.e., grain orientation and grain boundary characteristics) was investigated in detail for future implementation in pipeline steel production.

2. Material and experimental procedures

A microalloyed API X80 plate with the chemical composition listed in Table 1 was used in this study. Test samples (TS) of 19.1 × 6.0 × 2.0 mm (Fig. 1a) with original plate thickness (Fig. 1b) were extracted by wire cut and heat-treated in a DT1000 quenching dilatometer. In order to simulate the formation of distinct grain morphologies along the heat-affected zone (HAZ) of welded pipes, samples were austenitized and cooled at different rates using helium gas. Then, the resulting specimens with simulated weld region microstructure were subjected to the HIC test to investigate the susceptibility and

Table 1 – Chemical composition (%). X80 Plate.

C	S	Al	Si	P	Co	Ti+Nb+V
0.068	0.003	0.0243	0.193	0.019	0.0189	0.104
Cr	**Mn**	**Ni**	**Cu**	**Mo**	**Pcm**	
0.189	1.83	0.0165	0.0115	0.245	0.19	

HIC crack initiation and propagation mechanisms. The full austenitization temperatures were established at 900 °C for 1800 s to eliminate the microstructural banded zone. Bott et al. [14] investigated the effect of accelerated cooling at cooling rates of 1.5–20 $°C{\cdot}s^{-1}$ for X70 and X80 pipeline applications in Brazil in 2007. Then, they studied the microstructural evaluation of X80 pipeline steels under higher cooling rates up to 115 $°C.s^{-1}$ [15]. Although they covered a wide range of cooling rates in air, oil, and water, the institute specification only permitted cooling rates up to 40 $°C{\cdot}s^{-1}$ due to their controlling the final microstructure. Therefore, fully controlled cooling was performed using three different cooling rates of 0.5, 10, and 40 °C.s-1 to simulate coarse-grain heat-affected zone (CGHAZ) and inter-critical heat-affected zone (ICHAZ) microstructures of lowest mechanical and toughness properties [14,15]. It is notable that full thickness plate allows the study of the effect of micro-segregation on HIC behavior (Fig. 1).

X-ray diffraction (XRD) was performed on the samples, with Cu-Kα radiation (45 kV and 40 mA) in a diffractometer at continuous scanning mode at 2Θ between 40° and 100° and with a step of 0.02°. The Rietveld method [16] was used to calculate the weight percent of the phases. Dislocation density, micro-strain in the crystal lattice, and crystalline size could be estimated from the XRD pattern using Debye - Scherer's relation [17] and the Stoke Wilson formula [18]. The dislocation density (δ) was evaluated using the formula;

$$\delta = \frac{1}{D^2} \tag{1}$$

where D is Crystallite size associated with the relationship between crystallite size and peak broadening using Debye - Scherer's relation [17];

$$D = \frac{k\lambda}{\beta\cos\theta} \tag{2}$$

where k is shape factor that is equal to 0.9, λ is ray wavelength, β is Full width at half maximum (FWHM), and θ is X-ray diffraction angle in degrees. Also, micro-strain in the crystal lattice is calculated using the Stoke Wilson formula [18];

$$\varepsilon = \frac{\beta}{4\tan\theta} \tag{3}$$

HIC tests were carried out in H_2S-saturated NACE solution A (0.5%wt acetic acid and 5.0%wt NaCl dissolved in distilled water) by immersion as recommended by the NACE TM0284-2011 standard. As shown in Fig. 1, samples previously heat-treated in dilatometer (2 mm thin plates – Fig. 1a) and as-received samples (full thickness samples with 100 mm length and 20 mm width) were tested.

Arrangement: NACE solution was initially degassed with N_2 for 2 h and then 5 L were discharged into a sealed testing vessel, where the samples were previously positioned. Then supplementary N_2 was bubbled into the vessel followed by 1 h of H_2S saturation (200 ml/min/L). The test was performed at 25 °C for 96 h. After the HIC test, the samples were cleaned with distilled water and ethanol, and dried in a hot air stream. Then, the sample tests were sectioned in four parts in a precision diamond saw using lubricant, as recommended by NACE TM0284–2011 standard.

Afterwards, all samples at the plate transverse direction were sanded with up to #1200 emery paper, polished with diamond paste down to 1 μm, and then the microstructures were revealed by Nital 2 % etching. Finally, the microstructures and cracks were examined and analyzed by Optical Microscopy (OM), Scanning Electron Microscopy (SEM), Energy Dispersive Spectroscopy (EDS), and Electron Backscatter Diffraction Analysis (EBSD).

3. Results and discussion

Fig. 2 shows the SEM micrographs at transverse direction of the as-received and heat-treated specimens. The original as-received API X80 microstructure contained segregation bands through the centerline thickness plate constituted of martensite (M), bainite (B), degenerated pearlite (DP) and martensite-austenite microconstituent (M-A) on a banded Polygonal Ferrite (PF) matrix (Fig. 2 a, b). Nonmetallic inclusions smaller than 20 μm were found in the samples

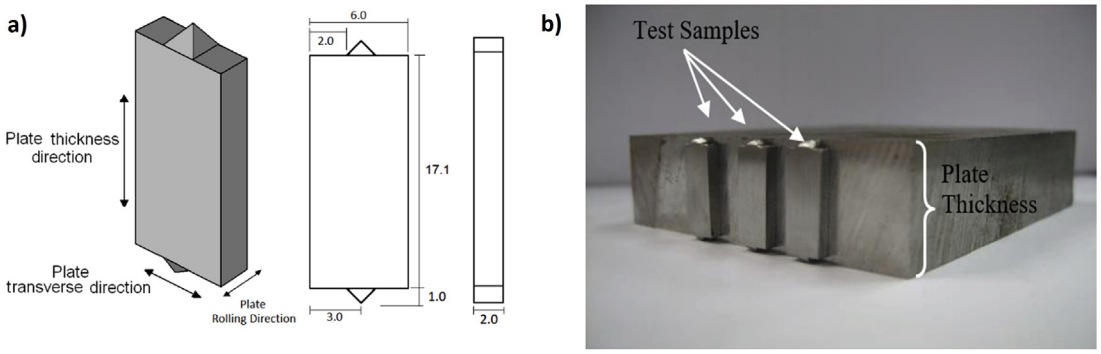

Fig. 1 – TS extracted from the plate. (a) Sketch of TS and its extraction orientation on the plate; (b) TS still attached to original plate. Measured in millimeters.

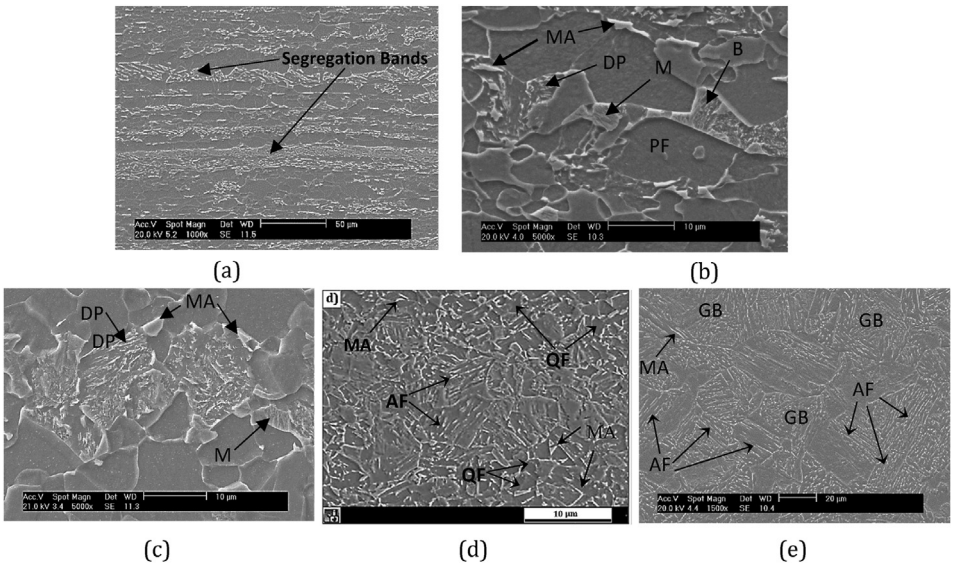

Fig. 2 – SEM micrographs of (a,b) original as-received API X80, and heat-treated specimens austenitized at 900 °C followed by three different cooling rates (c) 0.5 °C·s^{-1}, (d) 10 °C·s^{-1}, and (e) 40 °C·s^{-1} (Microstructure at plate transversal direction).

surface. Xiao et al. [19] reported that welding can generate stress concentration and defects such as cracks and oxide inclusion, promoting premature failure. Zhukov et al. [20] also pointed out that the presence of welding inclusions in the base metal enhances the formation of high degrees of residual deformation and micro discontinuities, resulting in pipeline failures along the weld joints. Microhardness average value varied from 231 ± 26 $HV_{0.1}$ in the surface to 306 ± 18 $HV_{0.1}$ in the segregation bands. Austenitized at 900 °C followed by cooling at a rate of 0.5 °C·s^{-1} revealed a sharp microstructural band (martensite, degenerated pearlite, and M-A micro-constituent) corresponding to the segregation remaining from solidification, mostly at the segregation bands (Fig. 2 c). The sample cooled at 0.5 °C.s^{-1} also exhibited the significant hardness variation from 205 ± 20 $HV_{0.1}$ to 305 ± 37 $HV_{0.1}$, from the surface through the segregation bands. It is well-known that the formation of an amount of banding zone increases HIC susceptibility by increasing the hydrogen trap sites [21–23]. In addition, microconstituents such as M, B, and DP deteriorate the HIC resistance due to the greater hardness than ferrite. With increasing the cooling rate, segregation bands microstructures were completely removed in the segregation bands. In addition, higher portions of refined acicular ferrite (AF), quasi-polygonal ferrite (QF), granular bainite (GB), and M-A microconstituent mainly originating from the prior austenite grain boundaries were observed in both samples cooled with 10 and 40C s^{-1} (Fig. 2 d, e). A higher amount of acicular ferrite and M-A was observed in samples cooled with 40 °C·s^{-1}. Acicular ferrite is often considered a form of very low carbon upper bainite, and can improve mechanical performance of pipework and pressure vessels [24]. A significant increment in the microhardness values was obtained in samples cooled with higher cooling rates. The microhardness increased to 346 ± 12 $HV_{0.1}$ in the sample cooled with 10 °C·s^{-1}, and reached the maximum microhardness values of 401 ± 6 $HV_{0.1}$ in the sample cooled with 40 °C·s^{-1}. The Vickers hardness values of investigated specimens are listed in Table 2. The presence of extensive center line segregation in the original as-received sample is mainly responsible for the high hardness variation in the samples (Fig. 1a). The segregation bands form during plate casting and solidification due to the rejection of solutes into surrounding liquid and the partitioning of solute elements to the mid-thickness of the plate with higher temperatures, which cause embrittlement and may cause unexpected cleavage fracture [25]. Similar hardness variation was observed in the sample cooled with the cooling rate of 0.5 °C.s^{-1}. However, the rapid cooling rate of 10 and 40 °C.s^{-1} could have effectively eliminated the formation of segregation bands and hardness variation as well. Also, a few numbers of non-metallic inclusions such as spherical CaO, CaS, and AlO–Ca inclusions were detected in all samples tested using EDS as shown in Fig. 3.

Fig. 4 shows XRD results of the original as-received ferritic X80, and cooled with different cooling rates. XRD patterns involving the peaks of (110) (200), and (211) planes correspond

Table 2 – The variation of Vickers hardness values at the surface and segregation bands of investigated specimens.

	Vickers hardness	
	Surface	Segregation bands
Original as-received API X80	231 ± 26 $HV_{0.1}$	306 ± 18 $HV_{0.1}$
Sample cooled with 0.5 °C/s cooling rate	205 ± 20 $HV_{0.1}$	305 ± 37 $HV_{0.1}$
Sample cooled with 10 °C/s cooling rate	346 ± 12 $HV_{0.1}$	354 ± 10 $HV_{0.1}$
Sample cooled with 40 °C/s cooling rate	401 ± 6 $HV_{0.1}$	408 ± 8 $HV_{0.1}$

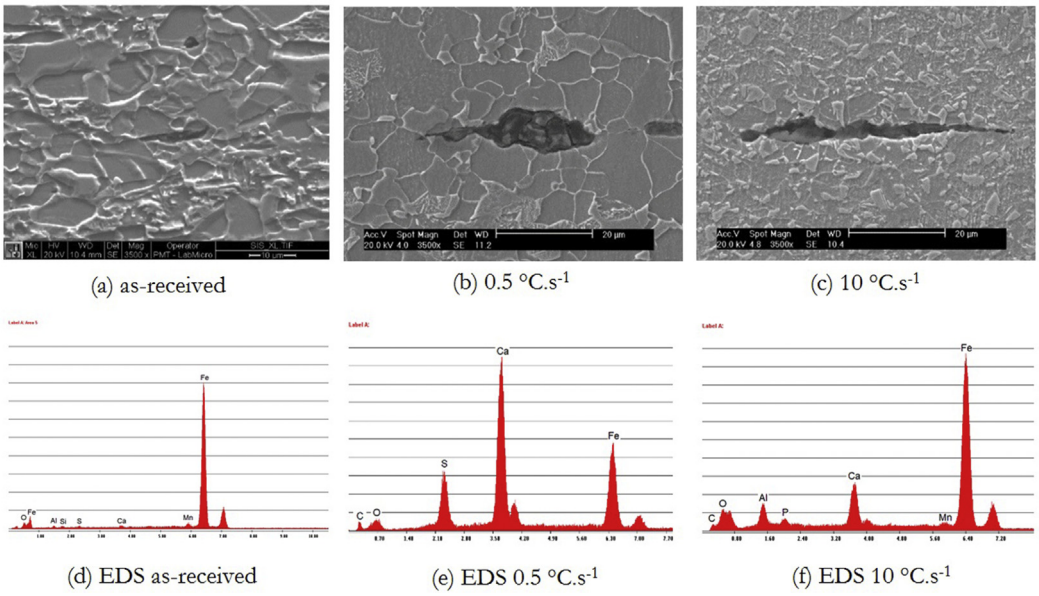

Fig. 3 – Typical inclusions observed in the samples tested (a) as-received, and samples cooled with (b) 0.5 °C.s^{-1}, and (c) 10 °C.s^{-1} cooling rate; chemical analyses using EDS for (d) EDS as-received, (e) EDS 0.5 °C·s^{-1}, and (f) EDS 10 °C·s^{-1}.

to BCC ferritic bainite phases for all samples, while about 5 % of (111)γ remaining austenite can be characterized. The volume fraction of retained austenite can be determined based on the integrated intensities of the BCC and FCC peaks as follows [26]:

$$V_\gamma = \frac{1.4I_\gamma}{I_\alpha + 1.4I_\gamma} = \frac{1.4\left[I_\gamma^{111}\right]}{\left[\frac{I_\alpha^{110}+I_\alpha^{200}}{2}\right] + 1.4\left[I_\gamma^{111}\right]}, \quad (4)$$

where I_γ and I_α are the integrated intensities of the diffraction lines of FCC austenite and BCC ferrite. The gradual dislocation density by increasing the cooling rate is presented in Fig. 5 and Table 3, which is consistent with the microstructure evolution.

After the HIC test, the specimens were sectioned in four parts in the transversal-normal direction (TD-ND) planes to reveal the crack through the mid-thickness of the specimens. Fig. 6a shows a long stepwise HIC crack preferentially propagated along the rolling direction located at the banded structure in the as-received API X80 steels. HIC cracks also propagated by interconnected stepwise cracking with a combination of small vertical and horizontal cracks. Although it is well-known that microcrack nucleation promotes the crack propagation through the mid-thickness regions, a detailed investigation to determine the role of grain orientation, grain boundary characteristics, and local strain distribution around crack propagation is essential to provide better understanding the HIC mechanisms.

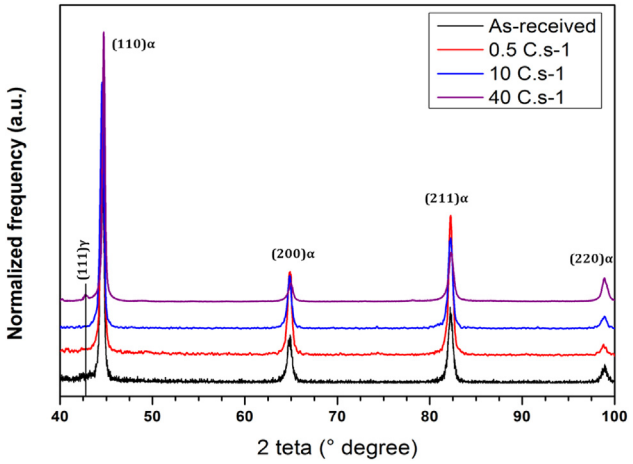

Fig. 4 – XRD patterns of all investigated specimens.

The sample cooled with the lowest cooling rate (0.5 °C·s^{-1}) exhibited the longest and widest HIC crack propagation mainly along the segregation zone in the mid-thickness of the plate, as expected. Fig. 6b shows the inhomogeneity of the microstructure around the HIC crack propagation in this sample. The central segregation banded zone contains harder phases, precipitates, and interphases. This high volume of boundaries produces hydrogen trapping sites which facilitate HIC nucleation and propagation [27]. The sample cooled with 10 °C·s^{-1} also showed some HIC crack propagation along ferritic microstructure (Fig. 6c). Some precipitates and inclusions such as MnS and Al–CaO were characterized inside the crack. The experiment to understand the behavior of hydrogen diffusion and trap hydrogen through steel using hydrogen permeation categorized the hydrogen traps into reversible and irreversible traps, regarding their binding energies and hydrogen retention capabilities. Grain boundaries and dislocations can store hydrogen due to lower binding energies (<60 kJ/mol), called the reversible traps. While, irreversible traps with higher binding energies (>60 kJ/mol) such as inclusions and precipitates permanently store hydrogen [28,29]. Jack et al. [29] reported that the reversible traps played a more important role in determining the HIC susceptibility of steels, due to diffusible

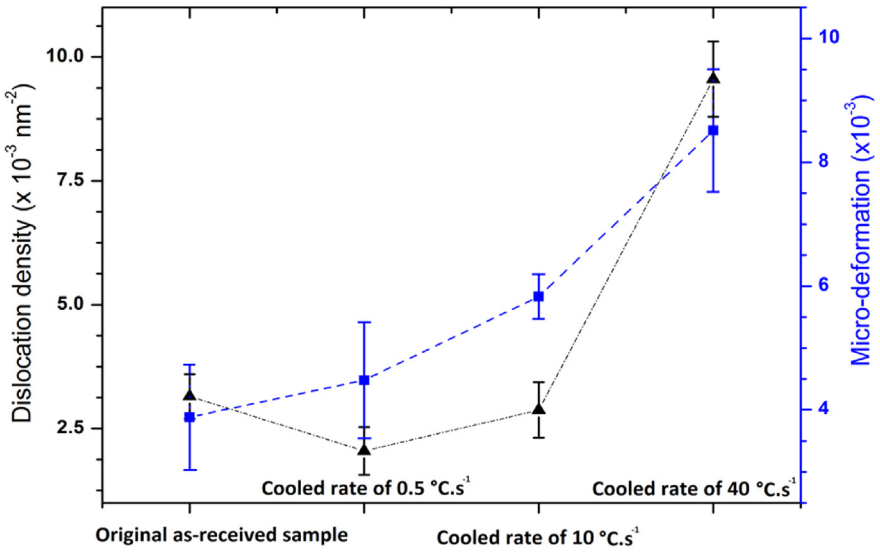

Fig. 5 – The variation of dislocation density and micro-deformation analyzed by XRD technique for all investigated specimens.

(mobile) hydrogen supply to stress concentration points within the steel matrix. They also showed that hydrogen atoms mainly transport along the grain boundaries, demonstrating their role in HIC cracks. In this case, both intergranular and transgranular crack modes were observed along the crack path at the middle of the plate thickness interconnected by inclusions. The examined areas of the sections of the specimens with the highest cooling rate (40 °C.s^{-1}), Fig. 6d, did not show any cracks or microcracks, indicating that the microstructures obtained by heat treatments are not sensitive to hydrogen induced cracking in a solution A sutured with H_2S according the NACE standard, which is the most severe test condition. The appropriate rapid cooling allows the formation of acicular ferrite and granular bainite with M-A refined and homogeneously distributed islands; the M-A distribution and size refined, when compared with less cooling rates, helps to reduce the hydrogen localized concentration delaying microcrack nucleation as well as microcrack interconnection. Zhao et al. [30] reported the superior HIC and sulfide stress cracking (SSC) resistance of acicular ferrite rather than ultrafine ferrite in H_2S environments. They explained that the high density tangled dislocations that the laths of acicular ferrite formed under a mixed diffusion and shear transformation mode result in preventing crack initiation. Moreover, the dispersion of probable M-A micro constituent as innocuous hydrogen traps [31] improves the redistribution of hydrogen and improves HIC resistance. Mohtadi-Bonab et al. [32] also documented that acicular ferrite has the most resistance against HIC. However, no relationship was provided to prove the influence of crystallographic features of the acicular ferrite matrix on the HIC phenomenon. Therefore, EBSD characterization was aimed to evaluate the possible effect of the crystallographic aspect on HIC resistance in this sample.

Table 3 – The variation of dislocation density and micro-deformation analyzed by XRD technique for all investigated specimens.

	δ x 10^{-3} (nm^{-2})	ε x 10^{-3}
Original as-received sample	3.146	3.8800
Cooled rate of 0.5 °C•s^{-1}	2.047	5.8338
Cooled rate of 10 °C•s^{-1}	2.870	4.4811
Cooled rate of 40 °C•s^{-1}	9.553	8.5199

The HIC stepwise crack is initiated from the brittle structures and non-metallic inclusions and then propagated along rolling direction at the segregation zone in the mid-thickness. The stepwise secondary cracks form at microstructural discontinuities mechanism was proposed by Ju and Rigsbee [33]. Microstructural discontinuities, such as crystal orientation, grain boundaries, and inclusion interphase, coupled with the presence of hydrogen, prioritizes the investigation of the stepwise cracking mechanisms. Fig. 7a shows the stepwise cracking propagated along rolling direction in segregation bands containing martensite, degenerated pearlite (DP), and M-A microconstituent for the as-received sample; this behavior was observed for the lowest cooling rate (0.5 °C•s^{-1}) in segregation bands containing martensite, degenerated pearlite with higher hardness (about 305 ± 37 $HV_{0.1}$) in comparison with the ferritic matrix (205 ± 20$HV_{0.1}$) (Fig. 7b and c). This provided an easy path for crack propagation due to the high concentration of hydrogen traps and brittle structure. Also, the external loading such as surrounding earth stability and the pressure inside the pipeline can accelerate crack propagation along the hard segregated zone. Such a considerable variation of hardness can be considered as an indicator of HIC susceptibility in H_2S environments. It is notable that the banded segregation zone contains a higher number of crystallographic defects such as hard phases and interphases, resulting in the formation of higher localized strain concentration. Localized strain concentration effectively increases the density of hydrogen traps, and consequently, will accelerate crack propagation.

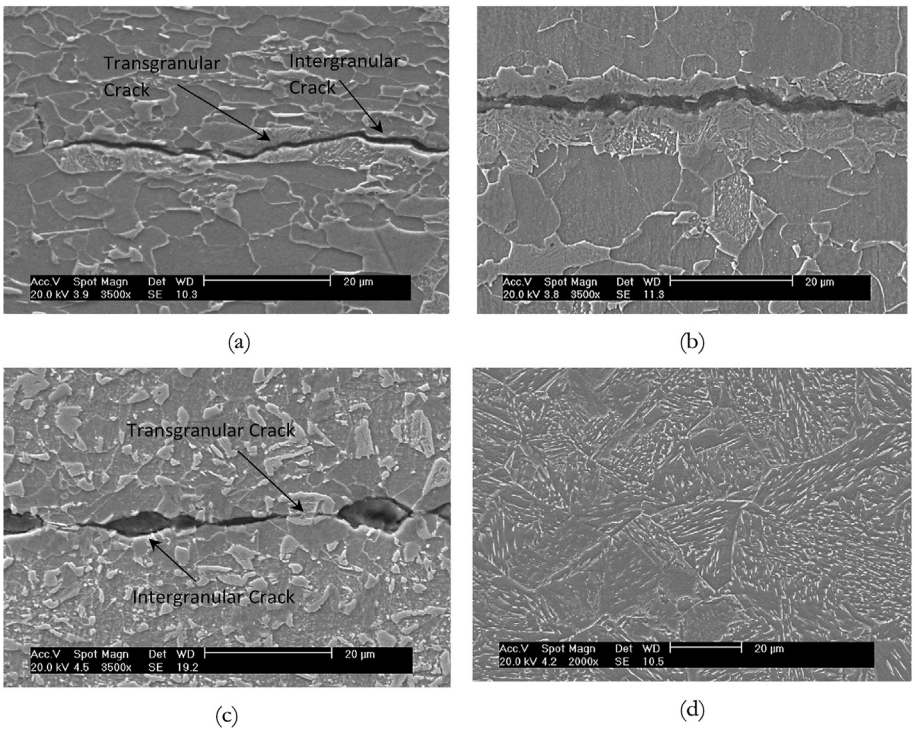

Fig. 6 – SEM micrographs of the sample (a) as-received and cooled with different cooling rates (b) 0.5 °C·s^{-1}, (c) 10 °C·s^{-1}, and (d) 40 °C·s^{-1} subjected to HIC test for 96 h.

The benefits of retained austenite from M-A micro-constituent in microalloyed steels, such as increasing ductility and fracture toughness, is well documented [34] and used regularly in DP steels, TRIP steels, and more recently, in carbide free bainitic steels and quenched & partitioning steels. Nevertheless, possible beneficial effects of the retained austenite with regard to hydrogen embrittlement are a controversial subject. A few authors, Shi et al. [35] in particular argued that M-A islands evenly distributed in a ferrite matrix allow a higher deformation, disrupting the propagation of cracks and consequently increasing the resistance to hydrogen-induced fracture. On the other hand, a large number of papers discuss the negative effects of the M-A micro-constituent, which acts as a preferred site for crack nucleation in the presence of hydrogen [10,21,22]. Retained austenite from M-A captures hydrogen present in low amounts in solid solution [10], increasing the internal stresses of austenite. In parallel, the accumulated hydrogen at the martensite/austenite interface forms molecules that generate pressure in the interface boundaries, forcing the austenite to activate plane-sliding mechanisms and deform in order to decrease the pressure at the M-A interface and avoid hydrogen-induced fracture. With increasing hydrogen concentration at the M-A interfaces and grain boundaries, after exhausting the plane sliding mechanisms the austenite will transform into strain-induced fresh martensite. The stresses arising from the volume expansion caused by the austenite to martensite transformation will add to the HE susceptibility; simultaneously hydrogen molecules weaken the interatomic cohesion force at the M-A and M-A/ferritic matrix interfaces, nucleating microcracks, as reported by Chen et al. [37], who also observed cracks at the austenite prior grain boundary. The nucleation and propagation of the cracks by hydrogen is more susceptible in regions with large, blocky M-A islands, while when the M-A particles are homogeneously distributed, they can avoid or delay the coalescence of microcracks, preventing their growth and subsequent fracture propagation. Microstructures consisting of predominantly acicular ferrite manage to distribute more evenly the M-A islands, thus increasing the HE resistance, as observed by [10]. The homogeneously distributed fine M-A islands may help to delay hydrogen fracture, but after a period of time, when local hydrogen saturations exceed a threshold, cracks do nucleate at these sites causing subsequent fracture.

The formation of stepwise HIC cracking depends on the interactions between the trapped hydrogen and the metallurgical state of the pipeline steel. The metallurgical and crystallographic defects determine the apparent solubility and the diffusion coefficient of hydrogen atoms. As the solubility of hydrogen in the Fe lattice is not very high, most of the hydrogen binds to trapping sites. The different traps are classified according to the binding forces between hydrogen and the trapping sites as “low”, “medium”, and “high” binding energy sites. Reversible trapping sites (0.20–0.40 eV) or medium bonding force correspond to semi-coherent precipitates. Dislocation cores, vacancies, high surface energy interphase surfaces, and crystallographic defects in general are responsible for irreversible or high-binding-energy trapping sites (0.45–0.62 eV) [24,25]. During operational service, atomic hydrogen is formed by corrosion reactions; usually the atomic

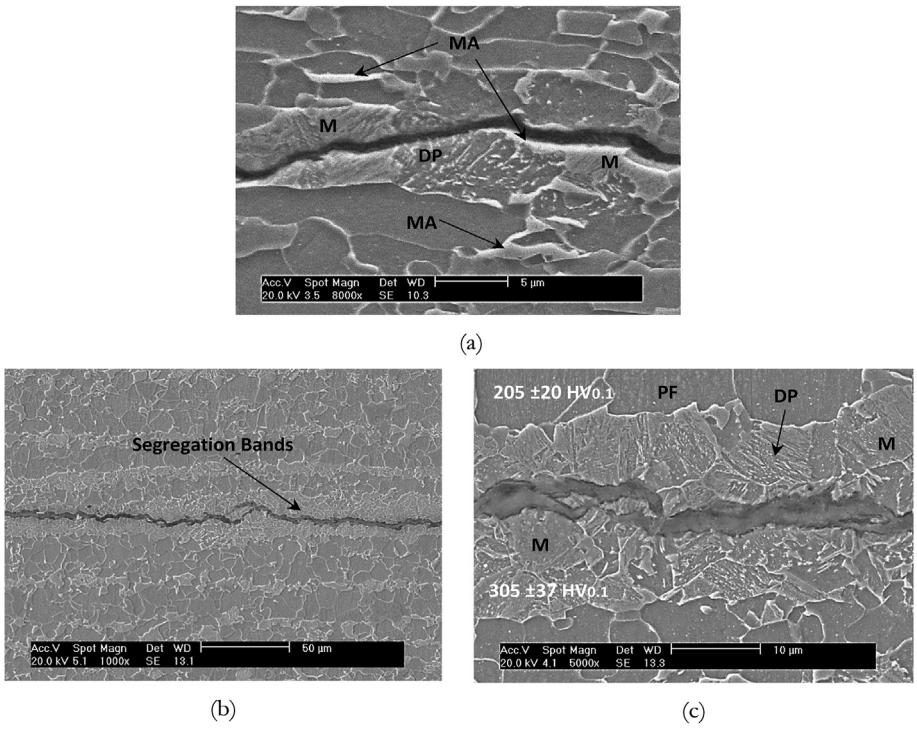

Fig. 7 – HIC crack propagation in sample: (a) as-received and (b) (c) submitted to slow cooling rate 0.5 °C/s submitted to HIC test.

hydrogen combines into H_2 molecules before defunding into the steel, but poisonous substances such as hydrogen sulfide (H_2S) retard the formation of H_2 molecules allowing the hydrogen atom to enter the steel [38]. The atomic hydrogen then diffuses into the component, until it is trapped into different microstructural and crystallographic defects. After some time, at suitable sites the hydrogen atoms start to recombine forming hydrogen molecules and an internal pressure is thus generated locally. Consequently, HIC initiates when the localized pressure within internal defects reaches the critical stress intensification factor K of the local matrix. The presence of segregation zones or bands increases the density of hydrogen traps, at the same time they provide defects and discontinuities like interphases, non-metallic inclusions and pores reducing the plasticity, contributing to formation and propagation of HIC cracks. This process is replicated in different places, and then, connected into a long continuous crack, originating the stepped crack morphology. Thus, the elimination of segregation zone during solidification process effectively can reduce HIC formation. The schematic crack nucleation and propagation mechanism along the segregation zone is presented in Fig. 8.

A higher amount of acicular ferrite and granular bainite appeared with the higher cooling rate (40 $°C \cdot s^{-1}$) in the simulated HAZ microstructure. A finer microstructure coupled with the absence of mid-thickness bands is developed. Specifically, no blisters at the surface and no HIC cracks were observed with the rapid cooling rate even after 96 h of exposure in an H_2S environment. It is also notable that the increase in the cooling rate could be caused by the formation of M-A microconstituents dispersed in refined structure, which can improve HIC resistance [40]. The refined structure reduces the local concentration of stress and hydrogen accumulation as well, thereby, preventing or diminishing both nucleation and propagation of cracks. As a consequence, accelerating the cooling of weld joints could increase toughness and HIC resistance. As mentioned earlier, type, geometry, distribution, and chemical composition of inclusions determine the HIC crack propagation.

Fig. 9b shows the normal direction orientation image map (OIM) obtained along the crack path in the mid-thickness of the as-received sample subjected to HIC test. Although the colorful OIM map indicates grain orientation, the exact crystallographic orientation distribution is obtained by orientation distribution function (ODF) associated with the volume percentage of each specific orientation in a polycrystalline specimen. ODF represents using three Euler angles (ϕ_1,φ,ϕ_2), which ODF at constant $\phi_2 = 45°$ exhibits the presence of the main crystallographic orientation in BCC materials. The ODF estimation revealed that rotated cube (001)<110> and Brass (110) $[1\bar{1}2]$ crystallographic orientations were predominant along the crack path in the mid-thickness region. The cleavage {001} grains mainly developed during hot rolling by recrystallization of austenite grains followed by ferrite transformation, have the largest interatomic spacing which promote hydrogen trapping and increases the local lattice distortion and consequently crack propagation [7,41]. Ohaeri et al. [42] also characterized the Brass texture component development during rolling process due to the austenite recrystallization, caused a drastic reduction in ductility and non-uniform HIC susceptibility.

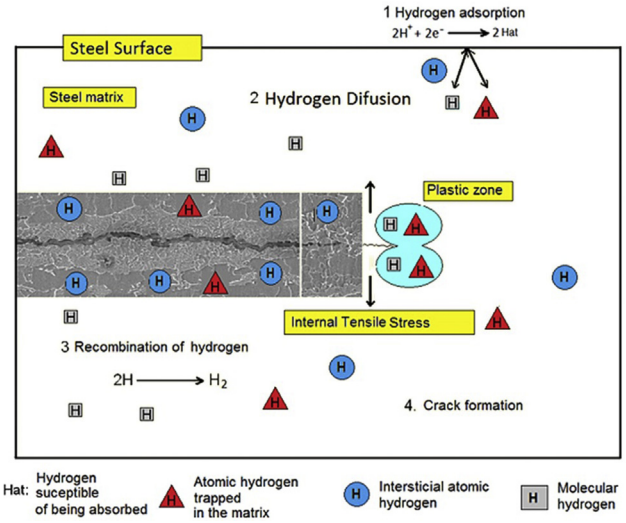

Fig. 8 – Crack nucleation and propagation mechanisms along the segregation band in microalloyed steel in the presence of hydrogen. Adapted from Hulka [39].

The more detailed normal direction orientation image along the crack path is shown in Fig. 10. It is clearly demonstrated that cracking propagated mainly along (001) and (101) grains parallel to the normal direction. From the above-mentioned EBSD analysis, the crack propagation, deflection, and arrest could be classified into three main important facts: (i) the crack mainly propagates along (101) parallel to the transverse direction (TD), known as the main slip plane in BCC structure, (ii) crack deflection observed in the (001) grains, which has the largest interplanar distance in bcc, consequently offers the easiest HIC crack trajectory, and finally (iii) the crack propagation was arrested close to the (111) grains.

The distribution of grain boundaries can control crack initiation and determine the behavior of crack propagation as well. The grain boundaries are categorized into three classes, i) low-angle boundaries (LABs) with point-to-point misorientation angle, $2^\circ < \Theta < 5^\circ$, ii) medium-angle boundaries (MABs) with misorientation angle, $5^\circ < \Theta < 15^\circ$, and iii) high-angle boundaries (HABs) with high point-to-point misorientation angle in the range of $15^\circ < \Theta < 62.5^\circ$, according the localized crystallographic distortion between neighboring pixels. The average point-to-point misorientation angle distribution and grain boundary distribution along the HIC crack path is shown in Fig. 11. The portion of LABs, MABs, and HABs was estimated at about 40.36, 20.38, and 39.26, respectively. Considering the accumulation of crystallographic defect within the grains (Fig. 9b and c), the crack might have been propagated easily in grains with higher level of deformation. Crack paths indicate predominantly transgranular crack propagation, the presence of some oriented grains {100} tend to be less severe the transgranular failure increasing the tendency for intergranular crack. Although high-angle high stored energy boundaries enhance crack propagation. Takasawa et al. [43] reported that increasing the number of HABs by grain refinement reduces the local hydrogen in the unit grain boundary area, consequently improving HIC crack resistance. Moreover, the formation of low and moderate boundaries can also reduce the stress distribution near the high angle boundaries, suppressing hydrogen-induced cracking initiation. In other words, the accumulation of crystallographic defects within the grains implies higher local stored energy for hydrogen trapping sites, and thus will facilitate crack propagation.

The Kernel average misorientation (KAM) effectively estimates the local plastic strain retained in the specimens by calculation of the average misorientation between a reference pixel and the 3rd nearest surrounding pixel within the same grain. Fig. 9d depicts the KAM map with misorientation angles less than 5° within the grain to estimate the dislocation density around the crack path. It is clear that the HIC crack propagated along regions with relatively high retention of residual stresses and high dislocation density associated with high local misorientation. Although some stress relieving treatments such as annealing can reduce the local residual stresses, this decreases mechanical properties (i.e., tensile strength and fracture toughness) which are essential for pipeline application. Thus, an appropriate manufacturing process to tailor the proper microstructure and local residual stresses is highly essential. The direct correlation between the increase in hydrogen traps with lattice defects and residual stresses was established, which resulted in increasing HIC susceptibility [29].

Taylor factor criterion investigate the level of plastic deformation due to the distribution of the grain orientation according to the slip planes [44]. For instance, grains already aligned in the slip planes easily slip when critical resolved shear stress is attained, while some grains undergo some kind of rotation to new positions in order to accommodate adequate slip planes. Therefore, Taylor factor exhibits a correlation between grain orientation and residual stresses induced during fabrication. It means soft grains with low Taylor factor contain less lattice distortion, while hard grains demonstrate higher density of lattice distortion due to the excessive rotation needed to activate the adequate slip systems. Thereby, Taylor factor analysis can determine the grains with higher HIC crack susceptibility due to the higher stored energy. Fig. 9e shows the Taylor map around the crack path. It is shown that the crack tends to propagate along the grains with high Taylor factors (marked in red colors) because these grains are less prone to slip.

In order to investigate how the acicular ferrite and granular bainite can increase HIC resistance, EBSD was measured in a simulated weld metal with 40 $^\circ C \cdot s^{-1}$ to investigate the grain orientation, grain boundary characteristics, local strain distribution, and Taylor factor. Fig. 12a and b shows the normal direction OIM and preferred crystallographic orientation developed in this condition. Rapid cooling rate of 40 $^\circ C.s^{-1}$ refines microstructure, increases the number of crystallographic defects, and enhances the formation of acicular ferrite and bainite with fine M-A micro constituents, discussed previously (Fig. 2e). A large volumetric fraction of about 58.08 % of MABs (misorientation between 5 and 15°) was estimated in this sample due to the ferrite laths interaction. MABs or subgrains work as a dislocation barrier inside the grains, prevent microcrack initiation and transgranular mode crack propagation. Lu et al. [45] suggested that possibly cracks cannot pass through these MABs, interrupting the crack growth. The proportions of LABs and HABs are also estimated as 17.33 and 24.58 %. The formation of parallel ferrite plates is

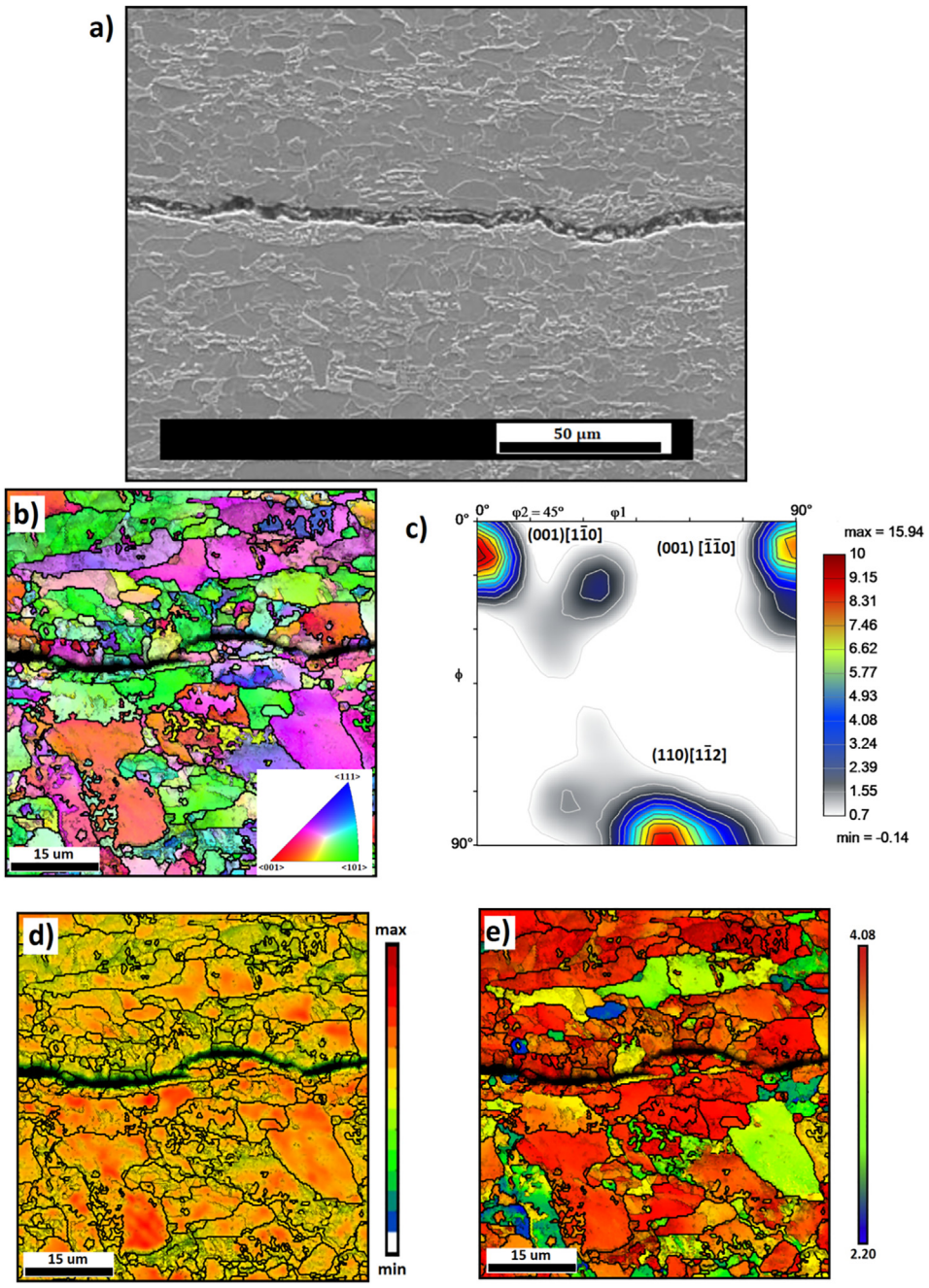

Fig. 9 – (a) SEM micrograph, (b) normal direction orientation image map, (c) orientation distribution function along HIC crack path (d) local strain distribution, and (e) Taylor factor map of as-received API X80 steel.

prevented by the fact that acicular bainite mainly nucleates intragranularly from inclusions inside the prior austenite grains [46]. From an atomic point of view, high angle boundaries with misorientation greater than 15° between two adjacent crystals contain a large number of dislocation arrays, indicating the large amount of the stored energy, and mainly contributes to crack propagation and HIC crack growth [47]. While, the higher moderate boundaries fraction attributed to the acicular bainite boundaries with lower stored energy can act i) increasing the number of hydrogen trapping sites without reaching the critical hydrogen saturation [29] and ii) acting as a crack growth barrier due to its lower brittleness, effectively can improve resistance to HIC failure. Therefore, the MABs formed in the acicular ferrite microstructure effectively act as crack propagation barriers and will increase crack propagation resistance. It can be concluded that the development of fine acicular ferrite consisting of fine interlocking plates with divergent crystallographic orientations prevents the formation of localized strain inside the grain and at grain boundaries in the presence of hydrogen. Crystallographic orientation analyses at constant $\phi_2 = 45°$ of ODFs revealed the weak cleavage (001)[$\bar{1}\bar{1}$0] and (111)[1$\bar{1}$0] orientation, while

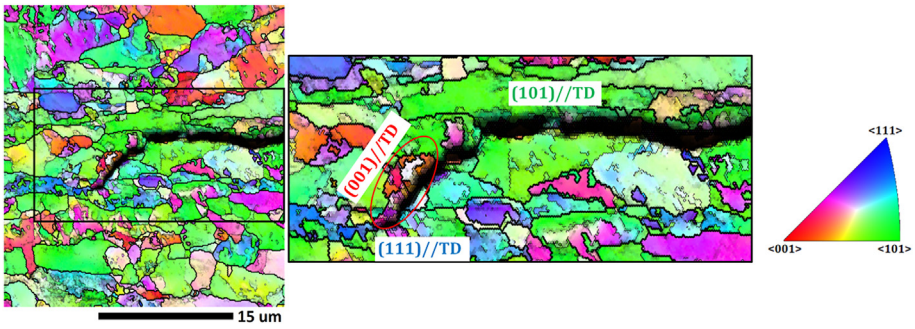

Fig. 10 – Normal direction orientation image map along hydrogen-induced cracks propagation, deflection, and arrest.

strong $(22\bar{1})[1\bar{1}0]$ is observed in this region (Fig. 12b). The presence of $(001)[\bar{1}10]$ orientation is attributed to the dynamic recrystallization of austenitic grains at elevated temperature. The development of $(111)[1\bar{1}0]$ and $(22\bar{1})[1\bar{1}0]$ orientations was reported as a result of displacive bainitic transformation of carbon-depleted zone at the prior austenite grain boundary, corresponding to the random crystallographic directions of bainite laths [48]. Evidence of such correlation between crystallographic orientation and grain boundary characteristics with superior HIC resistance could be sought for pipeline steel production in the future.

Fig. 12c shows the local strain distribution within the grains with a threshold of 5° to eliminate the effect of subgrain boundaries. Some regions with medium angle values around 5° within the grain are observed. Although these high angle values with high dislocation density are considered as traps for hydrogen atoms, refined structure interlocking ferritic plate prevent the formation of local strain concentration and consequently microcrack initiation. These high dislocation density regions are identified in grains oriented along (101) planes, known as compact planes in BCC structure. Thus, adequate slip systems could be accommodated for dislocation slipping to avoid the dislocation accumulation and microcrack formation as well. Taylor factor map, as a prediction of the level of plastic deformation according to the activated slip planes, is presented in Fig. 12d. A relatively lower deformation level in comparison with the as-received HIC-prone X80 can also compel higher HIC resistance to samples rapidly cooled from austenitization region. According to Mohtadi-Bonab et al. [6], grains with higher Taylor factors are prone to transgranular cracking while intergranular cracking forms between adjacent grains with a mismatch in Taylor factor. In this case, the HABs work as crack formation/propagation barrier due to divergent crystallographic orientations developed in acicular ferrite as was explained. Therefore, crystallographic aspects could explain how the acicular ferrite developed under a faster cooling rate exhibited superior HIC resistance.

Although HIC cracks were observed in the sample cooled with 10 $^{\circ}C\cdot s^{-1}$ cooling rate, the resulting homogeneous ferrite with granular bainite structure, with the absence of segregation zone bands improved HIC resistance in comparison with as-received and cooled slowly (0.5 $^{\circ}C\cdot s^{-1}$) samples. The presence of MnS and Al–CaO inclusions in the segregation zone in these conditions increases the hydrogen trapping site, possibly resulting in the formation of HIC crack in mid-thickness segregated region along the rolling direction. On the other hand, microstructures presenting refined acicular ferrite distributed within the grains, developed under a cooling rate of 40 $^{\circ}C\cdot s^{-1}$, successfully improved HIC resistance even after 96 h of exposure in an H_2S environment. The acicular ferrite mostly nucleates intragranularly in deformed austenite, then in growth according to the ability of carbon atoms to diffuse [36]. However, Santofimia et al. [49] reported that granular bainite nucleates mainly at poor-carbon austenite areas during isothermal holding as a result of stress fields associated with the grain boundaries. Therefore, the local strain misorientation result analyzed from the EBSD measurement of the sample cooled with 40 $^{\circ}Cs^{-1}$ cooling rate demonstrated about 35 ± 5 % of acicular ferrite in this structure. The formation of subgrain boundaries within the grains prevented localized strain concentration and hindered the formation of microcracks.

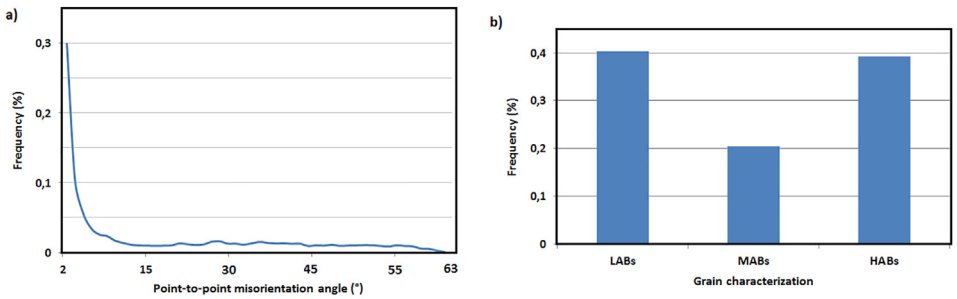

Fig. 11 – (a) Average point-to-point misorientation angle distribution and (b) grain boundary distribution along HIC crack path.

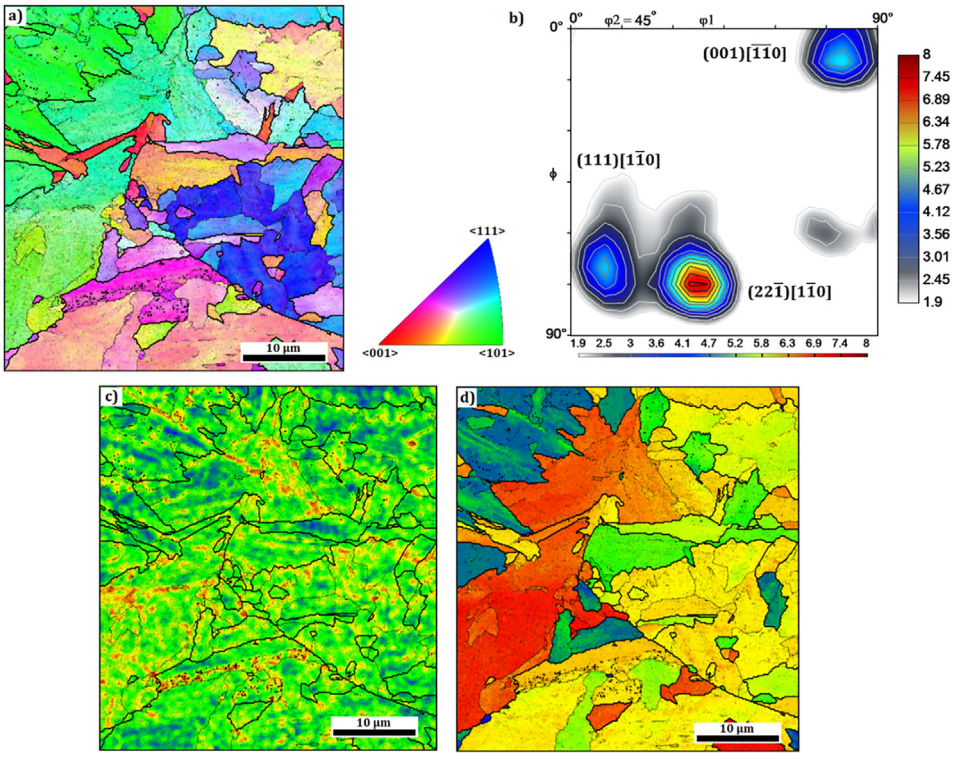

Fig. 12 – (a) OIM map, (b) ODF at constant $\phi_2 = 45°$, (c) local strain misorientation, and (d) Taylor factor map analyzed from EBSD measurement of sample cooled with 40 °C/s cooling rate.

4. Conclusions

This paper investigated the effect of cooling rates on hydrogen assisted cracking of X80 steel in terms of microstructure and crystallography. The results demonstrated that with increasing cooling rate, HIC sensibility decreases. The samples containing inclusions and segregation zone reduced HIC resistance, while the sample with fine acicular ferrite consisting of fine interlocking plates and divergent crystallographic orientations exhibited the best HIC resistance. In addition, microcrack initiation and transgranular crack propagation were suppressed by high proportion of medium-angle boundaries. The other conclusions are listed as follows:

- Cooling rates higher than 10 °C.s^{-1} can effectively eliminate the formation of micro segregation bands.
- Microsegregation bands consisting of brittle hard phases (like martensite and M-A) with some inclusions are the main source of crack initiation and propagation.
- The elimination of segregation band by heat treatment process can effectively reduce HIC crack formation
- The interface boundaries enhance localized internal energy, facilitating crack propagation.
- HIC crack propagates mainly along regions with relatively high residual stresses and high dislocation density associated with localized misorientation.
- The cleavage {001} grains mainly have the largest interatomic spacing, enhancing hydrogen trapping, increasing the local lattice distortion, and consequently accelerating crack propagation.
- The development of grains oriented along (101) planes provides adequate slip systems, consequently, reducing dislocation accumulation and microcrack formation.
- The formation of subgrain boundaries within the grains prevented localized strain concentration and hindered the formation of microcracks.

Declaration of Competing Interest

The authors declare that they have no known competing financial interests or personal relationships that could have appeared to influence the work reported in this paper.

Acknowledgements

The authors are grateful to CNPq - National Council for Scientific and Technological Development and to CAPES - National Coordination for Graduate Studies, in Brazil, for their financial support.

REFERENCES

[1] Mohammadijoo M, Valloton J, Collins L, Henein H, Ivey DG. Characterization of martensite-austenite constituents and micro-hardness in intercritical reheated and coarse-grained heat affected zones of API X70 HSLA steel. Mater Char 2018;142:321–31. https://doi.org/10.1016/j.matchar.2018.05.057.

[2] Arora KS, Pandu SR, Shajan N, Pathak P, Shome M. Microstructure and impact toughness of reheated coarse grain heat affected zones of API X65 and API X80 linepipe steels. Int J Pres Ves Pip 2018;163:36–44. https://doi.org/10.1016/j.ijpvp.2018.04.004.

[3] Qi Y, Luo H, Zheng S, Chen C, Lv Z, Xiong M. Comparison of tensile and impact behavior of carbon steel in H2S environments. Mater Des 2014;58:234–41. https://doi.org/10.1016/j.matdes.2014.01.065.

[4] Hejazi D, Haq AJ, Yazdipour N, Dunne DP, Calka A, Barbaro F, et al. Effect of manganese content and microstructure on the susceptibility of X70 pipeline steel to hydrogen cracking. Mater Sci Eng, A 2012;551:40–9. https://doi.org/10.1016/j.msea.2012.04.076.

[5] Venegas V, Caleyo F, Baudin T, Espina-hernández JH, Hallen JM. On the role of crystallographic texture in mitigating hydrogen-induced cracking in pipeline steels. Corrosion Sci 2011;53:4204–12. https://doi.org/10.1016/j.corsci.2011.08.031.

[6] Mohtadi-Bonab MA, Szpunar JA, Basu R, Eskandari M. The mechanism of failure by hydrogen induced cracking in an acidic environment for API 5L X70 pipeline steel. Int J Hydrogen Energy 2015;40:1096–107. https://doi.org/10.1016/j.ijhydene.2014.11.057.

[7] Masoumi M, Silva CC, Béreš M, Ladino DH, de Abreu HFG. Role of crystallographic texture on the improvement of hydrogen-induced crack resistance in API 5L X70 pipeline steel. Int J Hydrogen Energy 2017;42:1318–26. https://doi.org/10.1016/j.ijhydene.2016.10.124.

[8] Masoumi M, Silva CC, de Abreu HFG. Effect of crystallographic orientations on the hydrogen-induced cracking resistance improvement of API 5L X70 pipeline steel under various thermomechanical processing. Corrosion Sci 2016;111:121–31. https://doi.org/10.1016/j.corsci.2016.05.003.

[9] Khalili Tabas AA, Beidokhti B, Kiani-Rashid AR. Comprehensive study on hydrogen induced cracking of electrical resistance welded API X52 pipeline steel. Int J Hydrogen Energy 2020;24:289–302. https://doi.org/10.1016/j.ijhydene.2020.09.219.

[10] Park GT, Koh SU, Jung HG, Kim KY. Effect of microstructure on the hydrogen trapping efficiency and hydrogen induced cracking of linepipe steel. Corrosion Sci 2008;50:1865–71. https://doi.org/10.1016/j.corsci.2008.03.007.

[11] Saffari H, Shamanian M, Bahrami A, Szpunar JA. Effects of ERNiCr-3 butter layer on the microstructure and mechanical properties of API 5L X65/AISI304 dissimilar joint. J Manuf Process 2020;50:305–18. https://doi.org/10.1016/j.jmapro.2019.12.028.

[12] Omale JI, Ohaeri EG, Szpunar JA, Arafin M, Fateh F. Microstructure and texture evolution in warm rolled API 5L X70 pipeline steel for sour service application. Mater Char 2019;147:453–63. https://doi.org/10.1016/j.matchar.2018.12.003.

[13] Avila JA, Rodriguez J, Mei PR, Ramirez AJ. Microstructure and fracture toughness of multipass friction stir welded joints of API-5L-X80 steel plates. Mater Sci Eng, A 2016;673:257–65. https://doi.org/10.1016/j.msea.2016.07.045.

[14] Bott IS, Batista GZ, Hippert E, de Souza LFG, Rios PR. Brazilian high temperature processed steels for pipelines. In: Int. Symp. Microalloyed steels oil gas ind. TMS (The Minerals, Metals & Materials Society); 2007. p. 645–57.

[15] Bott IS, Vieira AAH, De Souza LFG, Rios PR. Microstructural evaluation of API 5L X80 pipeline steels submitted to different cooling rates. Mater Sci Forum 2010;638–642:3146–51. https://doi.org/10.4028/www.scientific.net/MSF.638-642.3146.

[16] Rietveld HM. A profile refinement method for nuclear and magnetic structures. J Appl Crystallogr 1969;2:65–71. https://doi.org/10.1107/S0021889869006558.

[17] Muramba V, Mageto M, Gaitho F, Odari V, Musembi R, Mureramanzi S, et al. Structural and optical characterization of tin oxide codoped with aluminum and sulphur. Am J Mater Sci 2015;5:23–30. https://doi.org/10.5923/j.materials.20150502.01.

[18] Parveen B, Khalid Z, Riaz S, Naseem S. Room-temperature ferromagnetism in Ni-doped TiO2 diluted magnetic semiconductor thin films. Rev Mex Trastor Aliment 2017;15:132–9. https://doi.org/10.1016/j.jart.2017.01.009.

[19] Xiao Y, Han Y, lin Yu E, Liu F, long Li D, Zhao Y qian. Formation of welding burrs on deep-sea oil pipe based on electromagnetic heating. Int Commun Heat Mass Tran 2019;108:104282. https://doi.org/10.1016/j.icheatmasstransfer.2019.104282.

[20] Zhukov D, Konovalov S, Melnikov A, Chen D. Evaluation of strength and microstructure of welded pipes with wall lamination. Eng Fail Anal 2021;122:105235. https://doi.org/10.1016/j.engfailanal.2021.105235.

[21] Nayak SS, Misra RDK, Hartmann J, Siciliano F, Gray JM. Microstructure and properties of low manganese and niobium containing HIC pipeline steel. Mater Sci Eng, A 2008;494:456–63. https://doi.org/10.1016/j.msea.2008.04.038.

[22] Beidokhti B, Dolati A, Koukabi AH. Effects of alloying elements and microstructure on the susceptibility of the welded HSLA steel to hydrogen-induced cracking and sulfide stress cracking. Mater Sci Eng, A 2009;507:167–73. https://doi.org/10.1016/j.msea.2008.11.064.

[23] Mohtadi-Bonab MA, Szpunar JA, Razavi-Tousi SS. A comparative study of hydrogen induced cracking behavior in API 5L X60 and X70 pipeline steels. Eng Fail Anal 2013;33:163–75. https://doi.org/10.1016/j.engfailanal.2013.04.028.

[24] Cruz-Chávez MA, Serna-Barquera SA, Juárez-Chávez J, Romero RJ, Cruz-Rosales MH, Campillo-Illanes B. Optimization-heuristic of mechanical properties of acicular ferrite steel. Mater Sci Eng, A 2018;721:65–73. https://doi.org/10.1016/j.msea.2018.02.076.

[25] Karani A, Koley S, Shome M. Failure of electric resistance welded API pipes – effect of centre line segregation. Eng Fail Anal 2019;96:289–97. https://doi.org/10.1016/j.engfailanal.2018.10.018.

[26] Li Z, Wu D. Effects of hot deformation and subsequent austempering on mechanical properties of high silicon and low silicon TRIP steel. Mater Sci Technol 2008;24:168–76. https://doi.org/10.1179/174328406X148750.

[27] Mohtadi-Bonab MA, Eskandari M, Szpunar JA. Texture, local misorientation, grain boundary and recrystallization fraction in pipeline steels related to hydrogen induced cracking. Mater Sci Eng, A 2014;620:97–106. https://doi.org/10.1016/j.msea.2014.10.009.

[28] Findley K, OBrien M, Nako H. Critical assessment 19: mechanisms of hydrogen induced cracking in pipeline steels. Mater Sci Technol 2016;32:8. https://doi.org/10.1179/1743284715Y.0000000131.

[29] Jack TA, Pourazizi R, Ohaeri E, Szpunar J, Zhang J, Qu J. Investigation of the hydrogen induced cracking behaviour of API 5L X65 pipeline steel. Int J Hydrogen Energy

2020;45:17671–84. https://doi.org/10.1016/j.ijhydene.2020.04.211.
[30] Zhao MC, Shan YY, Xiao FR, Yang K, Li YH. Investigation on the H2S-resistant behaviors of acicular ferrite and ultrafine ferrite. Mater Lett 2002;57:141–5. https://doi.org/10.1016/S0167-577X(02)00720-6.
[31] Zhao MC, Tang B, Shan YY, Yang K. Role of microstructure on sulfide stress cracking of oil and gas pipeline steels. Metall Mater Trans A Phys Metall Mater Sci 2003;34:1089–96. https://doi.org/10.1007/s11661-003-0128-7.
[32] Mohtadi-Bonab MA, Szpunar JA, Collins L, Stankievech R. Evaluation of hydrogen induced cracking behavior of API X70 pipeline steel at different heat treatments. Int J Hydrogen Energy 2014;39:6076–88. https://doi.org/10.1016/j.ijhydene.2014.01.138.
[33] Ju CP, Rigsbee JM. The role of microstructure for hydrogen-induced blistering and stepwise cracking in a plain medium carbon steel. Mater Sci Eng 1985;74:47–53. https://doi.org/10.1016/0025-5416(85)90109-0.
[34] Matlock DK, Speer JG, Moor 2E De, Gibbs PJ. Recent developments IN advanced high strength sheet steels for automotive applications: an overview. Jestech 2012;15:1–12.
[35] Shi X, Yan W, Wang W, Zhao L, Shan T, Yang K. Effect of microstructure on hydrogen induced cracking behavior of a high deformaility pipeline steel. J Iron Steel Res Int 2015;22:937–42. https://doi.org/10.1016/S1006-706X(15)30093-5.
[36] Pourazizi R, Mohtadi-Bonab MA, Szpunar JA. Investigation of different failure modes in oil and natural gas pipeline steels. Eng Fail Anal 2020;109:104400. https://doi.org/10.1016/j.engfailanal.2020.104400.
[37] Chen Y, Xu Z, Zhang X, Zhang T, Jackie J, Sun Z, et al. Irreversible hydrogen embrittlement study of B1500HS high strength boron steel. Mater Des 2021;199:109404. https://doi.org/10.1016/j.matdes.2020.109404.
[38] Mohtadi-Bonab MA, Mousavi H, Pourazizi R, Szpunar JA. Finite element modeling of HIC propagation in pipeline steel with regard to experimental observations. Int J Hydrogen Energy 2020;45:23122–33. https://doi.org/10.1016/j.ijhydene.2020.06.054.
[39] Hulka K. Sour gas resistant steel. Niobium information. Cia Bras Met e Mineração 2001;18:58–67.
[40] Sharma L, Chhibber R. Mechanical properties and hydrogen induced cracking behaviour of API X70 SAW weldments. Int J Pres Ves Pip 2018;165:193–207. https://doi.org/10.1016/j.ijpvp.2018.06.013.
[41] Béreš M, Wu L, Santos LPM, Masoumi M, da Rocha Filho FAM, da Silva CC, et al. Role of lattice strain and texture in hydrogen embrittlement of 18Ni (300) maraging steel. Int J Hydrogen Energy 2017;42:14786–93. https://doi.org/10.1016/j.ijhydene.2017.03.209.
[42] Ohaeri E, Eduok U, Szpunar J. Relationship between microstructural features in pipeline steel and hydrogen assisted degradation. Eng Fail Anal 2019;96:496–507. https://doi.org/10.1016/j.engfailanal.2018.11.008.
[43] Takasawa K, Wada Y, Ishigaki R, Kayano R. Effects of grain size on hydrogen environment embrittlement of high strength low alloy steel in 45 MPa gaseous hydrogen. Mater Trans 2010;51:347–53. https://doi.org/10.2320/matertrans.M2009241.
[44] Liu M, Yang CD, Cao GH, Russell AM, Liu YH, Dong XM, et al. Effect of microstructure and crystallography on sulfide stress cracking in API-5CT-C110 casing steel. Mater Sci Eng, A 2016;671:244–53. https://doi.org/10.1016/j.msea.2016.06.034.
[45] Lu W, Chakravarthula SS, Chen J, Qiao Y. Propagation of a cleavage crack front across a field of persistent grain boundaries. Int J Solid Struct 2012;49:584–9. https://doi.org/10.1016/j.ijsolstr.2011.11.003.
[46] Costin WL, Lavigne O, Kotousov A. A study on the relationship between microstructure and mechanical properties of acicular ferrite and upper bainite. Mater Sci Eng, A 2016;663:193–203. https://doi.org/10.1016/j.msea.2016.03.103.
[47] Takayama Y, Szpunar JA. Stored energy and taylor factor relation in an Al-Mg-Mn alloy sheet worked by continuous cyclic bending. Mater Trans 2004;45:2316–25. https://doi.org/10.2320/matertrans.45.2316.
[48] Guo H, Li Q, Fan Y, Feng X. Bainite transformation behavior, microstructural feature and mechanical properties of nanostructured bainitic steel subjected to ausforming with different strain. J Mater Res Technol 2020;9:9206–18. https://doi.org/10.1016/j.jmrt.2020.06.063.
[49] Ravi AM, Kumar A, Herbig M, Sietsma J, Santofimia MJ. Impact of austenite grain boundaries and ferrite nucleation on bainite formation in steels. Acta Mater 2020;188:424–34. https://doi.org/10.1016/j.actamat.2020.01.065.